ISSN 1674-1056
http://cpb.iphy.ac.cn
http://iopscience.iop.org/cpb
中国物理 B
Chinese Physics
中国物理 Chinese Physics B

Structural and electrical properties of carbon-ion-implanted ultrananocrystalline diamond films

Hui Xu(徐辉)[1], Jian-Jun Liu(刘建军)[1], Hai-Tao Ye(叶海涛)[2], D J Coathup[2], A V Khomich[3,4], Xiao-Jun Hu(胡晓君)[1]

Citation: Chin. Phys. B . 2018, 27(9): 096104. **doi:** 10.1088/1674-1056/27/9/096104

Journal homepage: http://cpb.iphy.ac.cn; http://iopscience.iop.org/cpb

What follows is a list of articles you may be interested in

Influences of annealing on structural and compositional properties of Al_2O_3 thin films grown on 4H-SiC by atomic layer deposition

Li-Xin Tian(田丽欣), Feng Zhang(张峰), Zhan-Wei Shen(申占伟), Guo-Guo Yan(闫果果), Xing-Fang Liu(刘兴昉), Wan-Shun Zhao(赵万顺), Lei Wang(王雷), Guo-Sheng Sun(孙国胜), Yi-Ping Zeng(曾一平)

Chin. Phys. B . 2016, 25(12): 128104. **doi:** 10.1088/1674-1056/25/12/128104

Low specific contact resistivity to graphene achieved by AuGe/Ni/Au and annealing process

Shu-Zhen Yu(于淑珍), Yan Song(宋焱), Jian-Rong Dong(董建荣), Yu-Run Sun(孙玉润), Yong-Ming Zhao(赵勇明), Yang He(何洋)

Chin. Phys. B . 2016, 25(11): 118101. **doi:** 10.1088/1674-1056/25/11/118101

Effects of Fe additive on diamond crystallization from carbonyl nickel powders-C system under HPHT condition

Li Yong, Jia Xiao-Peng, Feng Yun-Guang, Fang Chao, Fan Li-Juan, Li Ya-Dong, Zeng Xiang, Ma Hong-An

Chin. Phys. B . 2015, 24(8): 088104. **doi:** 10.1088/1674-1056/24/8/088104

Effects of annealing process on characteristics of fully transparent zinc tin oxide thin-film transistor

Chen Yong-Yue, Wang Xiong, Cai Xi-Kun, Yuan Zi-Jian, Zhu Xia-Ming, Qiu Dong-Jiang, Wu Hui-Zhen

Chin. Phys. B . 2014, 23(2): 026101. **doi:** 10.1088/1674-1056/23/2/026101

Investigation of the inhibiting outdiffusion of erbium atoms to a silicon-on-insulator surface after annealing at high temperature

Qin Xi-Feng, Li Hong-Zhen, Li Shuang, Ji Zi-Wu, Wang Hui-Ning, Wang Feng-Xiang, Fu Gang

Chin. Phys. B . 2012, 21(6): 066105. **doi:** 10.1088/1674-1056/21/6/066105

Structural and electrical properties of carbon-ion-implanted ultrananocrystalline diamond films*

Hui Xu(徐辉)[1], Jian-Jun Liu(刘建军)[1], Hai-Tao Ye(叶海涛)[2,†], D J Coathup[2], A V Khomich[3,4], and Xiao-Jun Hu(胡晓君)[1,‡]

[1] College of Materials Science and Engineering, Zhejiang University of Technology, Hangzhou 310014, China
[2] Aston Institute of Materials Research, School of Engineering and Applied Science, Aston University, Birmingham B4 7ET, United Kingdom
[3] V. A. Kotelnikov Institute of Radio-Engineering and Electronics, Russian Academy of Sciences, Moscow 141190, Russia
[4] National Research Nuclear University MEPhI, Moscow, Russia

(Received 13 April 2018; revised manuscript received 17 June 2018; published online 10 August 2018)

We investigate the structural and electrical properties of carbon-ion-implanted ultrananocrystalline diamond (UNCD) films. Impedance spectroscopy measurements show that the impedance of diamond grains is relatively stable, while that of grain boundaries (GBs) (R_b) significantly increases after the C^+ implantation, and decreases with the increase in the annealing temperature (T_a) from 650 °C to 1000 °C. This implies that the C^+ implantation has a more significant impact on the conductivity of GBs. Conductive atomic force microscopy demonstrates that the number of conductive sites increases in GB regions at T_a above 900 °C, owing to the formation of a nanographitic phase confirmed by high-resolution transmission electronic microscopy. Visible-light Raman spectra show that resistive trans-polyacetylene oligomers desorb from GBs at T_a above 900 °C, which leads to lower R_b of samples annealed at 900 and 1000 °C. With the increase in T_a to 1000 °C, diamond grains become smaller with longer GBs modified by a more ordered nanographitic phase, supplying more conductive sites and leading to a lower R_b.

Keywords: ultrananocrystalline diamond, C-ion implantation, annealing, electrical properties

PACS: 61.82.Rx, 81.05.U–, 81.05.uj, 81.07.–b **DOI:** 10.1088/1674-1056/27/9/096104

1. Introduction

Diamond films have excellent properties such as high hardness, good chemical stability, and high thermal conductivity.[1–3] Ultrananocrystalline diamond (UNCD) film is a unique form of carbon, in which diamond grains with sizes of 3–5 nm are surrounded by an amorphous carbon matrix. UNCD films have applications where high conductivities are required, including electrochemical electrodes,[4–6] field emission,[7] and heterostructures.[8,9] Extensive studies have been performed to improve the conductivities of UNCD films. It has been reported that nitrogen-doped UNCD films exhibit n-type conduction with an enhanced electrical conductivity, which is attributed to the increased number of sp^2 bonds at grain boundaries (GBs).[10,11] Phosphorous and oxygen ion implantations were used to increase the conductivity of nanocrystalline diamond grains and amorphous-carbon GBs, which improved the n-type Hall mobility of the UNCD film.[12,13] A hybrid structure of UNCD and graphene nanoribbons promoted a high mobility and n-type conductivity in an oxygen-ion-implanted UNCD film.[14] Lithium ion implantation induced the formation of electron trap centers inside diamond grains, whereas post-annealing healed the defects and converted the amorphous carbon phase into nanographite, forming conduction channels for an effective transport of electrons.[7]

Amorphous carbon in GBs is a common component in UNCD films, whose electrical conductivities were reported to be not sufficiently high, thus limiting the applications of UNCD films.[15] It is believed that the conversion of amorphous carbon to a conducting graphitic phase along GBs enhances the efficiency for electron transport on the surface, thus improving the conductivity of the UNCD film.[16,17] It was also reported that copper[18] and gold[19] ion implantations and annealing promoted electrical properties of UNCD films by decreasing the amorphous carbon content and even by inducing the nanographitic phase in GBs. This suggests that the electrical properties can be effectively improved by modifying the structure and component of amorphous-carbon GBs. Carbon ions are not dopants for diamond grains, but preferentially lead to more ordered amorphous-carbon GBs to enhance the conduction mobility. A high-dose C^+-ion implantation (10^{15} cm^{-2}) and annealing lead to crystallization of the

*Project supported by the National Natural Science Foundation of China (Grant Nos. 50972129 and 50602039), the International Science Technology Cooperation Program of China (Grant No. 2014DFR51160), the National Key Research and Development Program of China (Grant No. 2016YFE0133200), European Union's Horizon 2020 Research and Innovation Staff Exchange (RISE) Scheme (Grant No. 734578), One Belt and One Road International Cooperation Project from the Key Research and Development Program of Zhejiang Province, China (Grant No. 2018C04021), and Xinmiao Talents Program of Zhejiang Province, China (Grant No. 2017R403078).

†Corresponding author. E-mail: haitao.ye@leicester.ac.uk
‡Corresponding author. E-mail: huxj@zjut.edu.cn

© 2018 Chinese Physical Society and IOP Publishing Ltd

graphite phase that was not transformed from amorphous carbon in the UNCD film and degradation of the field-emission properties.[20] In this study, we implanted a lower dose of C^+ to regulate the microstructures of the UNCD films particularly in GBs to improve their electrical properties. High-resolution transmission electronic microscopy (HRTEM) and visible-light Raman spectroscopy were used to characterize the microstructures of the films after ion implantation and annealing. Conductive atomic force microscopy (AFM) was used to acquire images of conductive capacities at different parts of the UNCD films. Impedance spectroscopy (IS) was employed to distinguish the conductivity contributions from diamond grains and GBs.

The results show that the impedance resistance of GBs significantly increases after the C^+ implantation; it is effectively reduced with the increase in the annealing temperature (T_a) in the range of 650–1000 °C. The impedance of diamond grains is relatively stable. This suggests that the C^+ implantation has a larger impact on the impedance of GBs than on diamond grains. When T_a is above 900 °C, the number of conductive sites significantly increases in the GB region of the UNCD film owing to the formation of a nanographitic phase, which is responsible for the reduced impedance resistance of the GBs.

2. Experimental methods

UNCD films were deposited using a hot-filament chemical vapor deposition (HFCVD) system on single-crystal silicon (111) wafers. The carbon source was acetone, the volume ratio between acetone and hydrogen was 1%–2% with a total gas flow of 200 ml/min, the working pressure in the reaction chamber was 0.5–1.4 kPa, and the temperature of the substrate was approximately 850 °C. The thickness of the as-deposited UNCD films was approximately 5 μm, obtained at a growth rate of 1.5 μm/h. C^+ implantation was performed on as-deposited UNCD films with an implantation energy of 90 keV and dose of 10^{12} cm^{-2}. For room-temperature implantations, there is a universal critical damage density (10^{22} vacancies/cm^3), which, when exceeded, leads to complete graphitization of heavily damaged diamond crystals upon annealing.[21] It was shown that the C^+ implantation level of 10^{12} cm^{-2} at room temperature was significantly below the critical dose of (2–3)$\times 10^{15}$ cm^{-2}.[22] The implantation profile was determined by the Stopping and Range of Ions in Matter (SRIM-2013) software. C ions were implanted into diamond with an average ion range of 121 nm, creating 10^{19} vacancies/cm^3 in the meantime. The implanted samples were annealed at 500, 650, 725, 800, 900, and 1000 °C for 30 min at a pressure of 4000 Pa (80% N_2 and 20% O_2), denoted as C12500, C12650, C12725, C12800, C12900, and C121000, respectively. The annealing at 900 °C for 30 min was performed on an as-deposited UNCD film (sample 900-A) to distinguish the effects of C^+ implantation and annealing on the electrical properties of the UNCD films.

HRTEM was used to characterize the microstructures of the films using a Tecnai G2 F30 S-Twin microscope, produced by Philips-FEI. Visible-light Raman spectroscopy measurements (JobinYvon, Labor Raman HR-800) of the samples were performed with an excitation wavelength of 514 nm at room temperature. Conductive AFM and scanning Kelvin microscopy (SKM) were performed in a scanning probe microscope (SPM) (Solver P47, NT-MDT, Russia) under ambient conditions.

Ti (500 nm)/Au (300 nm) contacts were fabricated using an SPC-350 magnetron sputtering system with a metal mask covering on the UNCD films set before the deposition. The metal mask was fixed by a high-temperature tape with the UNCD film to ensure its stability during the deposition. The contacts were then annealed under a vacuum at 450 °C for 20 min. The diameter of the electrode was 2 mm. *I–V* measurements of the samples at room temperature showed that ohmic contacts were formed. The impedance properties of the samples were determined using an Autolab potentiostat–galvanostat connected with a four-probe station in the frequency range of 0.01 Hz to 10 MHz. IS was employed to study the electrical properties of single-crystal diamond and polycrystalline diamond. This technique involves a measurement of the real and imaginary components of the film impedance as a function of both frequency and temperature. The impedance as a complex number can be defined as

$$Z = Z' - \mathrm{j}Z'', \tag{1}$$

where the real part refers to the resistance contribution, while the imaginary part to the capacitance contribution. In a typical impedance spectroscopic analysis, the impedance is measured as a function of frequency, and the real component is plotted against the imaginary component with the change of the frequency. These so-called "Cole–Cole" plots may reveal different semicircular responses for each resistance–capacitance (RC) component of the film.[23]

Theoretically, a double RC parallel model in series could be used to simulate the electrical conduction of diamond films attributed to uniformly distributed diamond grains and GBs, as illustrated in Fig. 1. The resistance between the electrode and diamond films is considered during the measurements, denoted as R_e. In the figure, R_g, R_b, C_g, and C_b represent the resistances of diamond grains and boundaries, and capacitances of diamond grains and boundaries, respectively. Each parallel RC equivalent circuit model accurately fits the corresponding Cole–Cole semicircle. The employed fitting procedure is the same as that described by Kleitz and Kennedy, which enables us to determine the resistance and relaxation frequencies with a good precision.[24]

The complex impedance can be expressed as

$$Z' = R_e + \frac{R_g}{1+\omega^2 R_g^2 C_g^2} + \frac{R_b}{1+\omega^2 R_b^2 C_b^2}, \quad (2)$$

$$Z'' = \frac{\omega R_g^2 C_g}{1+\omega^2 R_g^2 C_g^2} + \frac{\omega R_b^2 C_b}{1+\omega^2 R_b^2 C_b^2}. \quad (3)$$

In the complex plane, the plot of Z' against Z'' has the form of two semicircles, where the contributions of diamond grains and GBs are easily identified. Therefore, the electrical conduction paths of the bulk material can be studied separately.

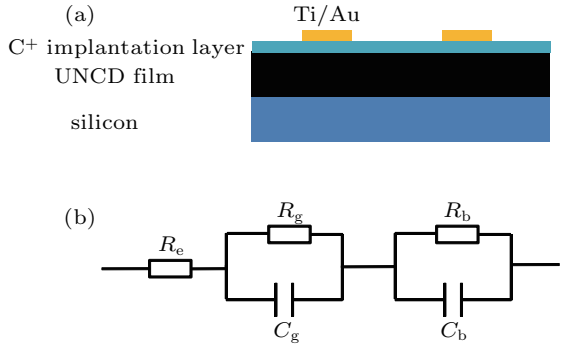


Fig. 1. (color online) (a) Schematic diagram of the electrical measurement across the film. (b) Equivalent circuit for the electrical response of a UNCD sample with contributions from diamond grains (denoted as "g"), grain boundaries (denoted as "b"), and electrode interface (denoted as "e").

3. Results and discussion

I–V measurements were performed before the IS measurements to ensure that ohmic contacts were formed between the electrodes and UNCD films. Figure 2 shows the Cole–Cole plots of the samples and Si substrate; as the Cole–Cole plot of the Si substrate is too small to be clearly observed, it is enlarged in the inset of Fig. 2(a). One semicircle is observed in the Cole–Cole plot of the Si substrate. The impedance is lower than 1 kΩ, which is 1–2 orders of magnitude lower than those of the annealed samples. This implies that the Cole–Cole plots of the samples mainly represent the electrical properties of the UNCD films. The Cole–Cole plots of all samples can be fitted by two semicircles, which indicates that two components contribute to the conductivity. The total impedance of the as-deposited sample is the lowest among the analyzed samples, approximately 28 kΩ. It increases to 62 kΩ for sample C12500 and 121 kΩ for sample C12650. It is worth noting that the semicircular response of sample C12725 is accompanied by an additional semicircle extending to low frequencies, in which the low-frequency response is incomplete and measured as an arc owing to the limited measuring range. Nevertheless, the total impedance of sample C12725 is estimated to be higher than that of sample C12500, but lower than that of sample C12650.

Figure 2(b) shows the Cole–Cole plots of samples 900-A, C12800, C12900, and C121000. The total impedance of sample 900-A is approximately 8 kΩ, which increases to 47 kΩ for sample C12800. With the increase in T_a above 800 °C, it decreases to 29 kΩ and 32 kΩ for samples C12900 and C121000, respectively. The impedance of sample 900-A is significantly lower than that of sample C12900, which indicates that the IS measurements effectively reveal the effect of the C^+ implantation on the electrical properties of the UNCD films, although the ion-implanted layer is thin, compared to the UNCD films. The total impedance of sample 900-A is lower than that of the as-deposited sample, which suggests that the annealing decreases the impedance of the UNCD film.

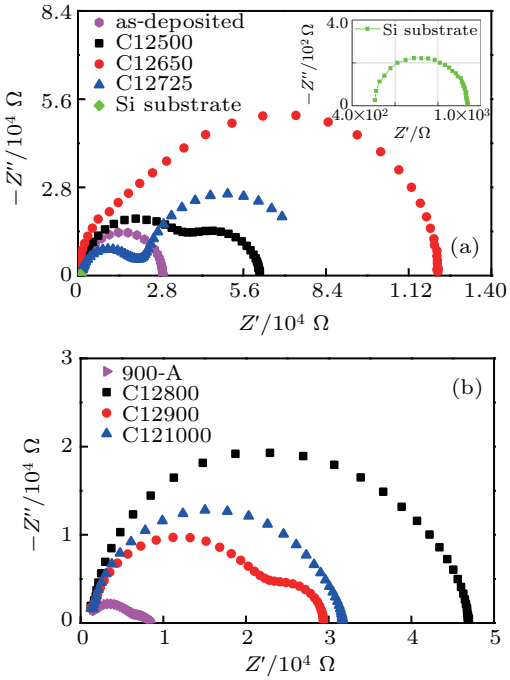


Fig. 2. (color online) Characteristic Cole–Cole plots measured for the (a) as-deposited sample, Si substrate, and samples C12500, C12650, and C12725, and (b) samples 900-A, C12800, C12900, and C121000.

The resistance and capacitance values were obtained according to the equivalent circuit model and presented in Table 1 to quantitatively understand the responses. The semicircular response at low frequencies corresponds to a capacitance value in the range of 0.2–9 nF, whereas the capacitance at the high-frequency region is 70–110 pF. It is well known that picofarad-scale capacitances for polycrystalline materials originate from the contribution of crystal grains, while nanofarad-scale responses are attributed to GBs.[25] Therefore, both nanocrystalline diamond grains and GBs in the UNCD films contribute to the measured electrical characteristics.

The R_e values presented in Table 1 are in the range of 1.4–1.7 kΩ, except that of sample C12650 (as the electrodes for sample C12650 were deposited by the vacuum evaporation method), which implies that the ohmic contacts are stable in these samples and that good conditions for IS measurements are provided. The R_g value of the as-deposited sample is 25.9 kΩ; it significantly decreases to 4.5 kΩ for sample 900-A. This implies that the annealing at 900 °C decreases the resistance of diamond grains in the UNCD films. It is worth

noting that the R_g of sample C12900 is 19.5 kΩ, significantly higher than that of sample 900-A, but lower than that of the as-deposited sample. In the C^+-implanted samples, the R_g value decreases from 33.4 kΩ to 18.9 kΩ with the increase in T_a from 500 °C to 725 °C. When T_a is above 800 °C, the R_g values of samples C12800, C12900, and C121000 are 27.3, 19.5, and 23.6 kΩ, respectively. The C^+ implantation increased the R_g of the UNCD films, without significant dependence on the annealing temperature.

Table 1. Resistance and capacitance values of the as-deposited sample, sample 900-A, and C^+-implanted samples.

Sample	R_e/kΩ	R_g/kΩ	C_g /pF	R_b/kΩ	C_b/nF
as-deposited	1.4	25.9	71.4	1.4	2.2
900-A	1.5	4.5	105.0	2.2	7.5
C12500	1.5	33.4	74.3	26.0	1.2
C12650	0.2	23.7	94.8	97.4	0.2
C12725	1.7	18.9	77.5	51.4	9.4
C12800	1.5	27.3	86.3	17.7	0.5
C12900	1.6	19.5	89.9	8.1	3.7
C121000	1.6	23.6	98.9	6.6	2.1

The R_b value of sample 900-A is 2.2 kΩ, slightly higher than that of the as-deposited sample of 1.4 kΩ. The R_b value of sample C12500 is 26 kΩ; it significantly increases to 97.4 kΩ for sample C12650. It starts to decrease when T_a further increases, reaching a value of 6.6 kΩ for sample C121000. These R_b values are higher than that of the as-deposited sample, which implies that the C^+ implantation increases the impedance of GBs even though it is effectively reduced by the annealing.

The IS results show that the contribution of diamond grains to the conductivity is increased after the C^+ implantation and annealing. The significantly increased R_b values of the C^+-implanted samples decrease with the increase in T_a in the range of 650–1000 °C, while the R_g values remain stable, which indicates that the C^+ implantation has a larger impact on the impedance of GBs. The lower R_b values of samples C12900 and C121000 show that their GB regions are more conductive than those of the C^+-implanted samples annealed at lower T_a.

In order to observe the conductive behavior at the microscale, conductive-AFM and SKM were employed. A Pt-coated Si cantilever with a tip curvature radius of ∼ 35 nm was used to obtain the surface height relief in the tapping mode. Local conductance was scanned in the contact mode across a previously detected surface-height-relief map (with a sample–probe gap of $\Delta = 0$). At each point, a bias voltage is applied between the sample and grounded probe to obtain the surface conductivity. Therefore, the local conductance represents the conductive behavior of the ion-implanted layer. A sample–probe gap of $\Delta = 100$ nm was used during the SKM measurements. For each sample, the measurements were repeated at 5 arbitrarily chosen 3×3 μm^2 regions. Figure 3 shows the surface height-relief and local conductance maps of samples C12725, C12900, and C121000. The surface height-relief maps show that the most probable relief heights of the samples increase with T_a, which indicates that the exposed area of nanoclusters becomes more significant at higher T_a. The local conductance maps show that the samples become more conductive with the increase in T_a. The most conductive areas in sample C12725 are scattered in the film; they become continuous in samples C12900 and C121000, which indicates that more conductive sites appear in these two samples. Combined with the IS results, we revealed that the R_g values of these three samples increase with T_a, while the R_b values decrease, which indicates that the conductive sites observed at the high T_a are mainly located at the GB regions.

Figure 4(a) shows the conductance histograms of samples C12725, C12900, and C121000. They show that the annealings at 900 °C and 1000 °C lead to ∼ 10 times higher conductances in the range of 100–500 nS compared to that of the sample annealed at 725 °C, which confirms the increased number of conductive sites. Figure 4(b) shows the contact-potential histograms of samples C12725, C12900, and C121000. The contact potentials of the samples increase with T_a, which implies loss of negative electron affinity at higher T_a.[26] This could be attributed to the absence of H-termination of nanocrystalline diamond grains when T_a is above 800 °C.[27–29]

The increased numbers of conductive sites in samples C12900 and C121000 indicate that the microstructure changes in the GB regions. In order to understand the origin of these highly conductive GBs, we performed HRTEM measurements to characterize the microstructures of the as-deposited sample and samples C12900 and C121000. During the TEM specimen preparation, first, the Si substrate was removed and then the UNCD film close to the Si side was removed by argon-ion milling, providing surface area (ion implantation region) for observation. Figures 5(a)–5(c) show low-magnification TEM images of the as-deposited sample and samples C12900 and C121000, and corresponding selected-area electron diffraction (SAED) patterns (insets), respectively. The SAED pattern of the as-deposited sample contains diffraction rings corresponding to the (111), (200), and (311) lattice planes of diamond, which indicates that diamond grains are the main component in the film. Many bright spots are observed on the diffraction rings, which implies that some large diamond grains exist in the film. The SAED patterns of samples C12900 and C121000 also contain diffraction rings corresponding to the (111), (200), and (311) lattice planes of the diamond. However, these rings are smooth without bright spots, which implies that the diamond grains in these samples are smaller and uniformly distributed. The grain sizes in the as-deposited sample are in the range of approximately 10–15 nm. They decrease to ∼ 5–10 nm in sample C12900 and become even smaller in sample C121000, providing more GB paths along the diamond grains.

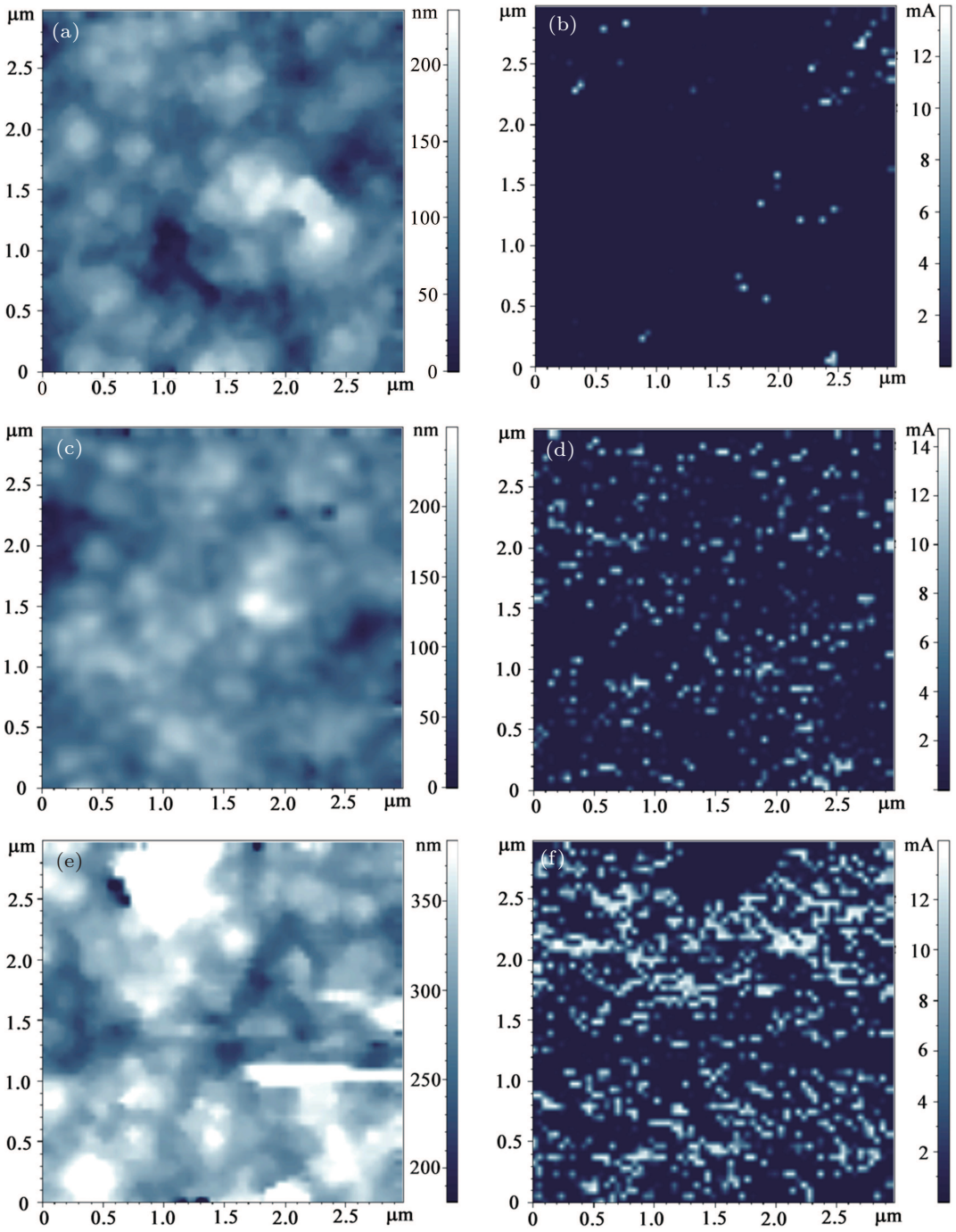


Fig. 3. (color online) Surface height-relief maps of samples (a) C12725, (c) C12900, and (e) C121000, and local conductances of samples (b) C12725, (d) C12900, and (f) C121000 at $U = 2$ V.

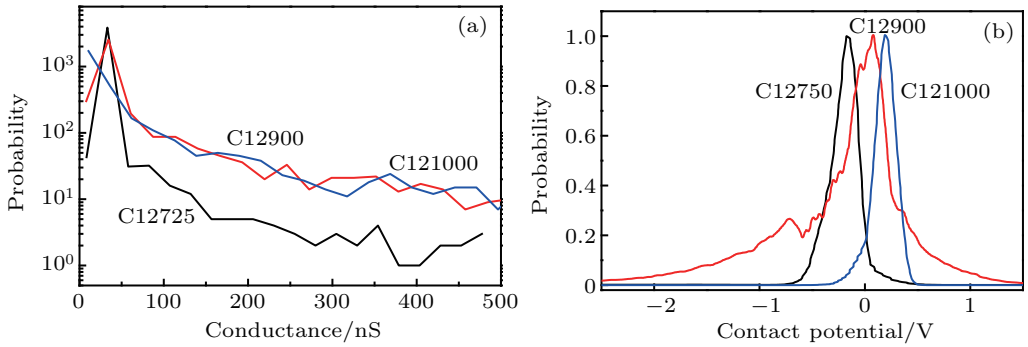


Fig. 4. (color online) (a) Conductance and (b) contact-potential histograms of samples C12725, C12900, and C121000 obtained from conductive-AFM measurements.

Figure 5(d) shows high-magnification TEM images of the as-deposited sample with Fourier-transform (FT) diffractograms corresponding to the entire image (FT_0), area 1 (FT_1), and area 2 (FT_2). The FT_0 image in Fig. 5(d) shows a ring with many spots and a circular bright spot in the center, which implies that amorphous carbon exists in the GBs of the as-deposited sample. The presences of diamond and amorphous carbon are demonstrated by images FT_1 and FT_2 corresponding to area 1 and area 2, respectively. The circular bright spot in the FT_1 pattern of area 1 is inversely transformed to provide insights into the GB microstructure, as shown in Fig. 5(d_1). The carbon clusters randomly intertwine in the GB area (representing the amorphous carbon). The FT_2 pattern is also inversely transformed in Fig. 5(d_2), which shows a lattice structure with a spacing of ~ 0.21 nm, reflecting the ordering of the (111) planes of the diamond.

Figure 5(e) shows high-magnification TEM images of sample C12900 with FT diffractograms corresponding to the entire image (FT_0), area 1 (FT_1), and area 2 (FT_2). The FT_0 image in Fig. 5(e) shows a ring with many spots and a central diffuse ring, which represent the diamond grains and GBs in sample C12900. The central diffuse ring in the FT_1 pattern of area 1 is inversely transformed in Fig. 5(e_1), which shows a different GB microstructure from that of the as-deposited sample. Some chain fringes are observed in the GBs. The spacing between the curved fringes is ~ 0.35 nm in Fig. 5(e_1), corresponding to the (0002) planes of the graphitic structure, which indicates that a nanographitic phase forms in the GBs of sample C12900. The FT_2 diffraction pattern is inversely transformed in Fig. 5(e_2), which shows a lattice structure with a spacing of ~ 0.21 nm, reflecting the ordering of the (111) planes of the diamond. Therefore, the spots in the diamond lattice ring of the FT_0 image represent nanocrystalline diamond grains in different orientations. The nanographitic phase in the GBs is less ordered than the diamond phase as no spots are observed in the corresponding graphite ring. The spots slightly deviate from the lattice ring, probably due to the diamond lattice damage by the ion implantation.

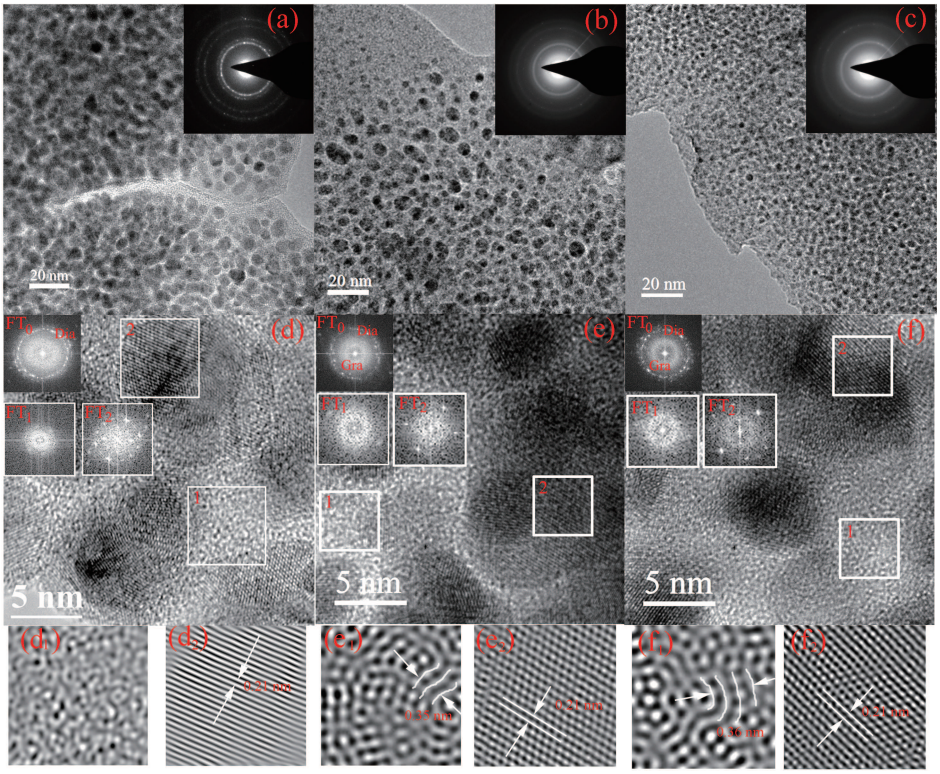


Fig. 5. (color online) Low-magnification TEM images and SAED patterns (insets) of the (a) as-deposited sample and samples (b) C12900 and (c) C121000. (d) High-magnification TEM image of sample C12900 with FT diffractograms corresponding to the entire image (FT_0), area 1 (FT_1), and area 2 (FT_2) (inset). (d_1), (d_2) Inversely transformed structures of amorphous-carbon and diamond diffraction points in area 1 and area 2, respectively. (e) High-magnification TEM image of sample C12900 with FT diffractograms corresponding to the entire image (FT_0), area 1 (FT_1), and area 2 (FT_2), shown in the inset. (e_1), (e_2) Inversely transformed structures of the graphite ring and diamond diffraction points in area 1 and area 2, respectively. (f) High-magnification TEM image of sample C121000 with FT diffractograms corresponding to the entire image (FT_0), area 1 (FT_1), and area 2 (FT_2) (inset). (f_1), (f_2) Inversely transformed structures of the graphite ring and diamond diffraction points in area 1 and area 2, respectively.

Figure 5(f) shows high-magnification TEM images of sample C121000 with FT diffractograms corresponding to the entire image (FT_0), area 1 (FT_1), and area 2 (FT_2). The density of spots in the diamond ring of the FT_0 image is higher than that of sample C12900, and the central ring corresponding to graphite is thinner, which demonstrates the smaller size of diamond grains and more ordered graphitic phase in sample C121000. The inversely transformed structures in Figs. 5(f_1)

and 5(f_2) show the orderings of the graphite (0002) and diamond (111) planes, respectively. The center area of the FT_2 image in Fig. 5(f) is significantly darker than those in Figs. 5(d) and 5(e), which implies that the amount of amorphous carbon is significantly lower in sample C121000. These HRTEM results confirm that diamond grains are the main component in the films, and that the GBs of the as-deposited sample mainly consist of amorphous carbon. In contrast, a nanographitic phase is formed in the GBs of samples C12900 and C121000, induced by the ion implantation and annealing. A more ordered nanographitic phase and more GB paths along smaller diamond grains exist in sample C121000 compared to those in sample C12900, in agreement with the lower R_b value of sample C121000. It can be concluded that the conductive sites observed in Figs. 3(e) and 3(f) are mainly formed by the nanographitic phase, attributed to the low-impedance GBs.

In order to further investigate the microstructure changes of GBs in the C^+-implanted samples, visible-light Raman spectra in the range of 800–2000 cm^{-1} for the as-deposited sample, sample 900-A, and C^+-implanted films are shown in Fig. 6(a). The Raman spectra of the UNCD films can be well fitted with six Gaussian–Lorentzian peaks. The peaks at 1550–1570 cm^{-1} and 1340 cm^{-1} correspond to the G- and D-bands, respectively.[30] The peak at 1332 cm^{-1} originates from diamond,[31] while that at 1200 cm^{-1} is related to amorphous sp^3 carbon.[32] In addition, two peaks are observed at 1140–1190 cm^{-1} (ω_1 peak) and 1480 cm^{-1} (ω_3 peak) attributed to bending and stretching vibrations of trans-polyacetylene (TPA) at the GBs of the UNCD films, respectively.[33]

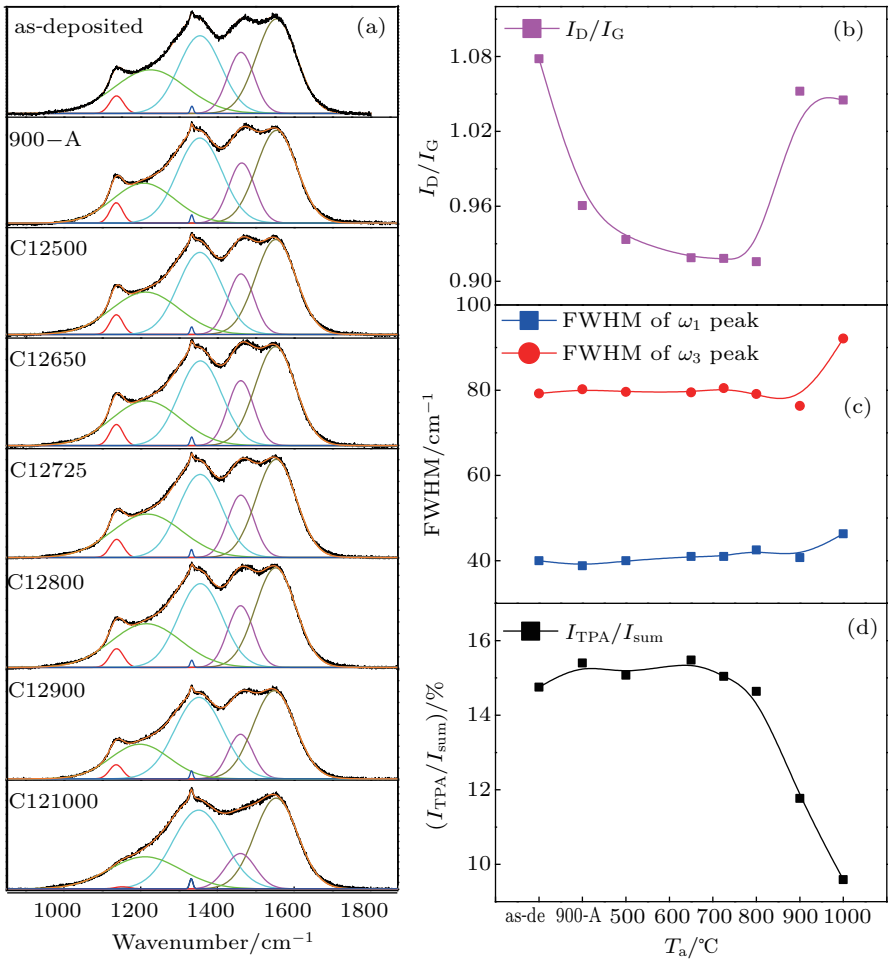


Fig. 6. (color online) (a) Visible-light Raman spectra of the C^+-implanted and as-deposited samples. (b) Dependences of I_D/I_G on T_a. (c) Dependences of the FWHM values of the ω_1 and ω_3 peaks on T_a. (d) Dependences of I_{TPA}/I_{sum} on T_a.

Figure 6(b) shows the I_D/I_G values (intensity ratio between the D and G bands) as a function of T_a, obtained from the fitted peaks in Fig. 6(a). The I_D/I_G value of the as-deposited sample is the highest (1.07), which decreases after the annealing at 900 °C (0.96). It becomes lower in the T_a range of 500–800 °C (0.91–0.93) and then increases at higher T_a ($\sim$ 1.05) for the C^+-implanted samples. This indicates that the size of the sp^2-bonded carbon located at GBs decreases at 500–800 °C and then increases at 900–1000 °C.[34,35] This is consistent with the result that the nanographitic phase forms conductive sites in samples C12900 and C121000. Figure 6(c) shows the dependences of the full-width-at-half-maximum (FWHM) values of the ω_1 and ω_3 peaks on T_a. They are stable when T_a is lower than 900 °C and increase at larger

temperatures. The I_{TPA}/I_{sum} values of the samples annealed at 500–725 °C (15.0%–15.5%) are slightly higher than that of the as-deposited sample (14.75%). The value is lower for sample C12800 (14.6%), while those of samples C12900 (11.8%) and C121000 (9.6%) are significantly decreased, as shown in Fig. 6(d). This implies that TPA oligomers in GBs start to desorb when T_a is higher than 800 °C, in agreement with the contact-potential result. TPA chains, as one of the π-conjugated polymers, are non-conductive without dopants.[36] It was reported that more TPA dangling bonds in UNCD films led to a high sheet resistance.[37] After the annealing at 1000 °C, the FWHM values of the ω_1 and ω_3 peaks increase, while the I_{TPA}/I_{sum} ratio significantly decreases, which is consistent with the lower R_b of sample C121000 than that of sample C12900.

IS results show that the R_g is relatively stable, while the R_b significantly increases after the C^+ implantation, which indicates that the contribution of diamond grains is increased after the ion implantation. The R_b gradually decreases with the increase in T_a in the range of 650–1000 °C, which implies that the C^+ implantation has a larger impact on GBs than on diamond grains. The IS and AFM results demonstrate that the number of conductive sites in the GBs increases with T_a in the range from 725 °C to 1000 °C. The HRTEM and AFM results demonstrate that the number of conductive sites in GBs increases at T_a higher than 900 °C owing to the formation of the nanographitic phase. Visible-light Raman spectra and HRTEM results show that the nanographitic phase is more ordered in sample C121000 than that in sample C12900, which provides more conductive sites and leads to the lower R_b of sample C121000.

4. Conclusion

We showed that the C^+ implantation significantly increased the impedance resistance of GBs, which was effectively reduced with the increase in T_a in the range of 650–1000 °C, while the impedance resistance of diamond grains was relatively stable in UNCD films. This suggested that the C^+ implantation had a larger impact on the impedance of GBs than on that of diamond grains. Conductive-AFM results demonstrated that the number of conductive sites in GBs significantly increased when T_a was above 900 °C owing to the formation of a nanographitic phase, confirmed by HRTEM. Visible-light Raman spectra and HRTEM results showed that the nanographitic phase was more ordered in sample C121000 than in sample C12900, which further decreased the R_b of sample C121000.

References

[1] Kundrat V, Zhang X, Cooke K, Sun H, Sullivan J and Ye H 2015 *AIP. Adv.* **5** 473

[2] Li X, Ye J S, Zhang H C, Feng T, Chen J Q and Hu X J 2017 *Appl. Surf. Sci.* **412** 366

[3] Yang T, Wei Q, Qi Y and Yu Z 2015 *Diamond Relat. Mater.* **52** 49

[4] Wang J, Firestone M A, Auciello O and Carlisle J A 2004 *Langmuir* **20** 11450

[5] Garrett D J, Ganesan K, Stacey A, Fox K, Meffin H and Prawer S 2012 *J. Neural. Eng.* **9** 016002

[6] Jiang M Y, Yu H, Li X, Lu S H and Hu X J 2017 *Electrochim. Acta* **258** 61

[7] Sankaran K, Srinivasu K, Yeh C, Thomas J, Drijkoningen S, Pobedinskas P, Sundaravel B, Leou K C, Leung K T, Van Bael M K, Schreck M, Lin I N and Haenen K 2017 *Appl. Phys. Lett.* **110** 261602

[8] Zkria A and Yoshitake T 2016 *Compound Semiconductor Week, Includes 28th International Conference on Indium Phosphide & Related Materials (IPRM) & 43rd International Symposium on Compound Semiconductors (ISCS)*, June 26–30, 2016, Toyama, Japan, p. 2016

[9] Zimmermann T, Kubovic M, Denisenko A, Janischowsky K, Williams O A, Gruen D and Kohna E 2005 *Diamond Relat. Mater.* **14** 416

[10] Panda K, Sundaravel B, Panigrahi B, Magudapathy P, Nandagopala Krishna D, Nair K, Chen H C and Lin I N 2011 *J. Appl. Phys.* **110** 044304

[11] Zapol P, Sternberg M, Curtiss L A, Frauenheim T and Gruen D M 2001 *Phys. Rev. B* **65** 045403

[12] Hu X J, Ye J S, Liu H J, Shen Y G, Chen X H and Hu H 2011 *J. Appl. Phys.* **109** 053524

[13] Hu X J, Ye J S, Hu H, Chen X H and Shen Y G 2011 *Appl. Phys. Lett.* **99** 131902

[14] Hu X J, Chen C K and Lu S H 2016 *Carbon* **98** 671

[15] Sankaran K J, Panda K, Sundaravel B, Chen H C, Lin I N, Lee C Y and Tai N H 2012 *ACS. Appl. Mater. Inter.* **4** 4169

[16] Sankaran K J, Lin Y F, Jian W B, Chen H C, Panda K, Sundaravel B, Dong C L, Tai N H and Lin I N 2013 *ACS Appl. Mater. Inter.* **5** 1294

[17] Arenal R, Bruno P, Miller D, Bleuel M, Lal J and Gruen D 2007 *Phys. Rev. B* **75** 195431

[18] Sankaran K, Panda K, Sundaravel B, Tai N and Lin I N 2014 *J. Appl. Phys.* **115** 063701

[19] Sankaran K J, Kunuku S, Sundaravel B, Hsieh P Y, Chen H C, Leou K C, Tai N H and Lin I N 2015 *Nanoscale* **7** 4377

[20] Joseph P, Tai N, Chen C, Niu H, Cheng H, Pong W and Lin I N 2009 *J. Phys. D: Appl. Phys.* **42** 105403

[21] Uzan Saguy C, Cytermann C, Brener R, Richter V, Shaanan M and Kalish R 1995 *Appl. Phys. Lett.* **67** 1194

[22] Prawer S and Kalish R 1995 *Phys. Rev. B* **51** 15711

[23] Bevilacqua M, Tumilty N, Mitra C, Ye H, Feygelson T, Butler J E and Jackman R B 2010 *J. Appl. Phys.* **107** 033716

[24] Kleitz M, Kennedy J, Vashishta P, Mundy J and Shenoy G 1979 *Fast Ion Transport in Solids* (Noth Holland: Elsevier) p. 185

[25] Mcdonald J R, 1987 *Impedance Spectroscopy Emphasizing Solid Materials and Systems* (Wiley)

[26] O'Donnell K M, Edmonds M T, Tadich A, Thomsen L, Stacey A, Schenk A, Pakes C I and Ley L 2015 *Phys. Rev. B* **92** 035303

[27] Liao M, Liu J, Sang L, Coathup D, Li J, Imura M, Koide Y and Ye H T 2015 *Appl. Phys. Lett.* **106** 083506

[28] Ueda K, Kasu M, Yamauchi Y, Makimoto T, Schwitters M, Twitchen D J, Scarsbrook G A and Coe S E 2006 *IEEE Electron. Dev. Lett.* **27** 570

[29] Xu H, Ye H T, Coathup D, Mitrovic I Z, Weerakkody A D and Hu X J 2017 *Appl. Phys. Lett.* **110** 033102

[30] Xiao X, Birrell J, Gerbi J E, Auciello O and Carlisle J A 2004 *J. Appl. Phys.* **96** 2232

[31] Lespade P, Al-Jishi R and Dresselhaus M S 1982 *Carbon* **20** 427

[32] Prawer S, Nugent K W, Jamieson D N, Orwa J O, Bursill L A and Peng J L 2000 *Chem. Phys. Lett.* **332** 93

[33] Vlasov I I, Ralchenko V G, Goovaerts E, Saveliev A V and Kanzyuba M V 2006 *Phys. Status Sol. A* **203** 3028

[34] Chhowalla M, Ferrari A, Robertson J and Amaratunga G 2000 *Appl. Phys. Lett.* **76** 1419

[35] Ferrari A C and Robertson J 2004 *Philos. T. R. Soc. A* **362** 247

[36] Conwell E, Mizes H and Jeyadev S 1989 *Phys. Rev. B* **40** 1630

[37] Alcantar-Peña J J, Montes J, Arellano-Jimenez M J, Aguilar J O, Berman-Mendoza D, García R, Yacaman M J and Auciello O 2016 *Diamond Relat. Mater.* **69** 207